

Electrodeposition of carbon cloth supported Co-Mo-B bifunctional catalytic electrode for water splitting

Fu Wang^{1,2, #}, Xuwei Zhu^{1, #}, Jialun Shi³, Yucheng Wu^{1,2}, Sensen Xin^{2, *}, Xiaofeng Wei^{1, *}, Wei Su⁴, Qiongyu Zhou⁵, Minqi Sheng^{3, *}

¹ College of Mechanical and Electronic Engineering, Northwest A&F University, Yangling 712100, China

² Guangdong Midea Kitchen & Bathroom Appliances Co.,Ltd. ,Foshan 528000, China

³ Shagang School of Iron and Steel, Soochow University, Suzhou 215021, China

⁴ School of Physic and Electronic Science, Zunyi Normal University, Zunyi, 563006, China

⁵ School of Materials Science and Energy Engineering, Foshan University, Foshan 528000, China

F. Wang and X. Zhu contributed equally to this work.

*E-mail: sensen.xin@midea.com (S.Xin), wxf8412@nwafu.edu.cn (X. Wei), shengminqi@suda.edu.cn (M. Sheng)

Received: 1 November 2020 / Accepted: 26 December 2020 / Published: 31 January 2021

Water splitting has attracted increasing global interest due to its ability of produce high purity hydrogen, but lack of non-noble metals based bifunctional catalysts with highly active for both hydrogen evolution and oxygen evolution reaction (HER and OER) substantially hinders its applications in large-scale. In this work, we propose a facile approach to fabricate a self-supported Co-Mo-B/CC electrode, via electrodepositing amorphous Co-Mo-B spheres on the carbon cloth (CC) supports. The prepared Co-Mo-B/CC electrode possesses comparable catalytic activity for HER with a low overpotential of 84.5 mV at -10 mA cm⁻² (cathodic current density). Meanwhile, it displays high activity for OER with 92.6 mV at 10 mA cm⁻² (anodic current density). In addition, the two-electrode electrolysis system of Co-Mo-B/CC(-)//Co-Mo-B/CC(+) exhibits a quite low cell voltage of 1.694 V to drive $j_{\text{cell}} = 10 \text{ mA cm}^{-2}$ for overall water splitting and outstanding durability, which makes it a promising bifunctional electrocatalyst for both the HER and OER.

Keywords: Co-Mo-B, Carbon cloth, Water splitting, Hydrogen evolution reaction, Oxygen evolution reaction

1. INTRODUCTION

The development of our society requires renewable, clean energy to confront the energy crisis and environmental pollution caused by humankind activities and continuous depletion of fossil fuels [1,

2]. To date, Hydrogen (H_2) is supposed to be an ideal energy carrier due to its high energy density, renewability and pollution-free [3, 4]. A considerable prospective approach for producing high purity hydrogen is water splitting, which consists of two half reactions at the cathode (hydrogen evolution reaction, HER) and anode (oxygen evolution reaction, OER) [5, 6]. Therefore, design and fabrication of bifunctional catalysts with high activity and excellent stability, which can expedite reaction kinetics and increase energy conversion efficiency of both HER and OER, remains a highly desirable goal, particularly with respect to the economical non-noble metals based catalysts [7-10].

Recently, 3d-transition metal borides (TMBs) have attracted renewed attention due to their superior catalytic properties, good stability, easy accessibility, and relative low cost [11]. Numbers mono-metal borides such as Co-B [12], Ni-B [13], Fe-B [14] have been discovered effective activity for HER (or OER), though far from the state of replacing noble metals in commercial applications. Besides, ternary TMBs such as Ni-Co-B, Co-Fe-B, Ni-Mo-B would show much superior electrochemical activity to their mono-metallic counterparts in general, due to the synergy effect between the two metal elements [15-17]. However, in order to increase the electrochemical active surface area and then improve the catalytic performance, many of the reported TMBs catalysts are low dimension nano materials [18, 19], which show low stability owing to their peculiarities of easy agglomeration at high current densities [20]. In addition, these materials should be assembled on the electrode surface by conductive additives and polymers binders, which would decrease the active surface area, consequently lower the catalytic activity [5, 21]. These two aspects dramatically limit the real applications of low dimension TMBs. An efficient strategy to address these shortcomings is in situ fabricating the TMBs catalysts on the conductive upholder [22-24].

Carbon cloth (CC), which owns large specific surface area, good flexibility and can provide good electrical conductivity, stable support architecture, has been widely studied as electrode materials [25-27]. In this paper, we report a one-step strategy to fabricate carbon cloth supported Co-Mo-B (Co-Mo-B/CC) bifunctional catalytic electrode via electrodeposition technology. The as-prepared Co-Mo-B/CC electrode with a stable structure exhibits a higher catalytic activity and outstanding stability in alkaline medium.

2. EXPERIMENTAL

2.1 Fabrication of Co-Mo-B/CC and Co-B/CC electrodes

The Co-Mo-B catalysts were electrodeposited on the CC supports, which had been cut into 1×1 cm^2 , and activated in a mixed acid solution ($V_{H_2SO_4}:V_{HNO_3}=3:1$) for 3 h. Then the CC supports were vertically immersed into the plating solution containing $CoSO_4 \cdot 7H_2O$ (0.2 mol/L), $Na_2MoO_4 \cdot 2H_2O$ (0.06 mol/L), $Na_2B_4O_7 \cdot 10H_2O$ (0.3 mol/L) and $Na_3C_6H_5O_7 \cdot 2H_2O$ (0.2 mol/L). The pH value of the solution was adjusted by NaOH and sulfuric acid to be 6.7 ± 0.1 , and the solution temperature maintained at 60 ± 1 °C during the process of electrodeposition.

Pulse electrodeposition technology was carried out to fabricate the Co-Mo-B catalyst. The current density, pulse duty cycles, pulse frequencies, deposition time are 4 mA/cm^2 , 70 %, 1000 Hz and

30 min, respectively. Afterwards, the obtained Co-Mo-B/CC electrode was rinsed with deionized water and ethanol several times and dried at 60 °C under vacuum for 8 h. Co-B/CC electrode was also fabricated as the contrast sample under identical synthesis conditions, but without adding $\text{Na}_2\text{MoO}_4 \cdot 2\text{H}_2\text{O}$ into the plating solution.

2.2 Characterization

The crystalline structure and micro-morphological information morphology of the fabricated electrodes were characterized by X-ray diffractometer (XRD, Rigaku Ultima IV, $\text{Cu K}\alpha$ radiation with $\lambda=1.5406 \text{ \AA}$), field-emission scanning electron microscope (FESEM, Hitachi SU5000) and transmission electron microscope (TEM, FEI Tecnai G220), respectively. The element composition analysis was carried out by X-ray spectrometry (EDX, Oxford X-act) in SEM mode. The chemical states of elements were disclosed using X-ray photoelectron spectroscopy (XPS, Thermo Fisher Model ESCALAB 250Xi) with monochromated $\text{Al K}\alpha$ radiation.

2.3 Electrochemical measurements

All electrochemical measurements were tested with Princeton VersaSTAT 4 electrochemical analyzer using a three-electrode configuration in 1.0 M KOH solution. Before each test, the KOH solution was purified by blowing N_2 for 15 min. The as-fabricated Co-Mo-B/CC (or Co-B/CC) electrode was used as the working electrodes. Hg/HgO/OH^- (1.0 M) electrode and graphite rod were used as the reference and counter electrodes, respectively. For comparison, The RuO_2 and Pt/C dip-coated on CC (denoted as RuO_2/CC and Pt/C/CC) were also used as the working electrodes. The mass loadings of RuO_2 and Pt/C were 0.35 mg cm^{-2} , which is the same mass as that of Co-Mo-B/CC.

3. RESULTS AND DISCUSSION

The morphology and elements distribution of designed Co-Mo-B/CC electrode is recorded with SEM-EDS (Fig. 1a). It can be observed that the nodular Co-Mo-B spheres compactly cover the entire surface of CC, and the Co, Mo, B, O elements within the Co-Mo-B spheres are uniformly distributed over the CC. TEM image gives an insight into the morphology of Co-Mo-B/CC electrode showing the small Co-Mo-B spheres (80~100 nm) are well arranged in series, which can ensure a good structural stability and connectivity (Fig. 1b). The HR-TEM image and SAED patterns demonstrate the Co-Mo-B spheres are amorphous (Fig. 1c). In addition, the broad diffraction peak at around $2\theta=45^\circ$ in the XRD pattern for the Co-Mo-B/CC electrode can also confirm the natural amorphous properties of Co-Mo-B spheres (Fig. 1d). The content of Co, Mo, B is ca. 50.4 at.%, 24.2 at.%, 13.6 at.%, respectively (Fig. 2). The remaining is slight C and O, which would arise from the electrodeposition process in an aqueous solution [28, 29]. Diffraction signals from CC substrates are also existent in the Co-Mo-B/CC composite

electrode patterns. The unsaturated bonds in amorphous structures can serve as active sites, which is supposed to be favorable HER and OER [30, 31].

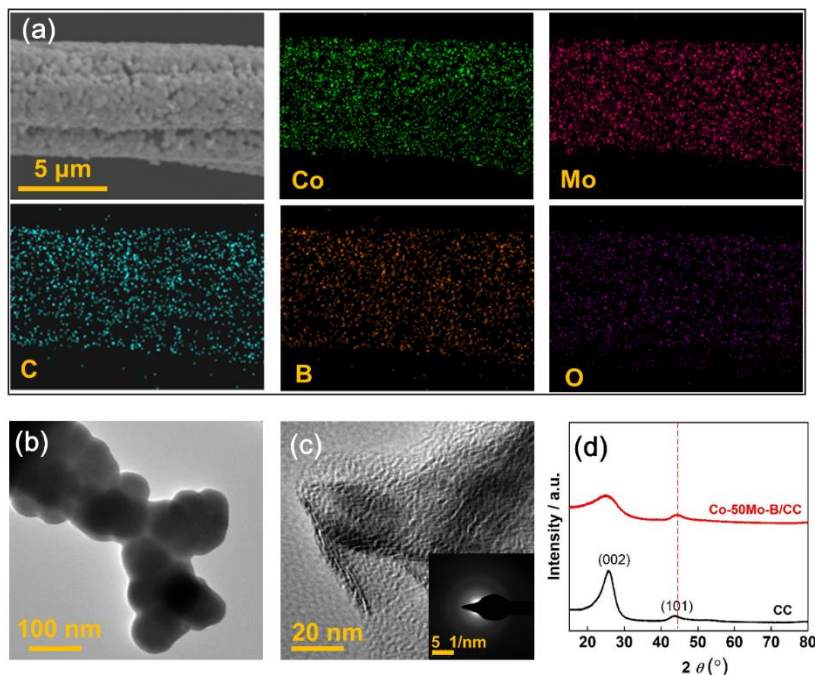


Figure 1. (a) SEM image and the corresponding EDX elemental maps of Co, Mo, C, B and O over the Co-Mo-B/CC electrode; (b) TEM image and (c) HR-TEM images, SAED pattern (inset of c) the Co-Mo-B spheres in the Co-Mo-B/CC electrode; (d) XRD pattern of the Co-Mo-B/CC electrode and CC supports.

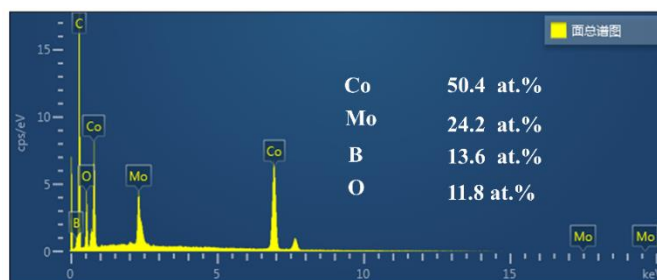


Figure 2. EDS spectrum and chemical composition of Co-Mo-B/CC electrode

The chemical states of Co-Mo-B/CC electrode are investigated by using XPS. As shown in the survey XPS spectrum (Fig. 3), there exists Co, Mo, B, O and C elements in Co-Mo-B/CC electrode. The Co 2p high-resolution spectrum (Fig. 4a) exhibits metallic Co⁰ (780.6 eV, 796.3 eV) and oxidized Co²⁺ (782.3 eV, 797.6 eV) [32, 33]. The Mo 3d XPS spectrum (Fig. 4b) displays metallic Mo⁰ (227.0, 231.0 eV) without obvious Mo oxides [34]. The B1s XPS spectrum (Fig. 4c) reveals both metallic B⁰ (187.7 eV) and oxidized B³⁺ (191.9 eV) [18, 30]. The B⁰ peak position is higher than that of for pristine B (187.0 eV), due to the electron transfer from B to Co and Mo [35]. The peak located at 530.3 eV corresponds to the signals of metal B-O-metal (Co, Mo) in Co-Mo-B (Fig. 4d) [34, 35].

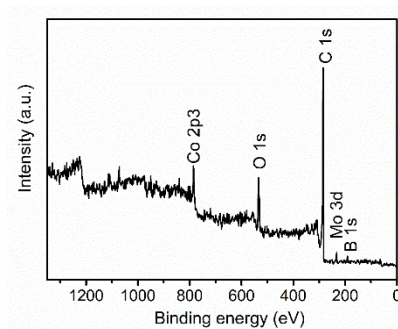


Figure 3. The survey XPS spectrum of Co-Mo-B/CC electrode

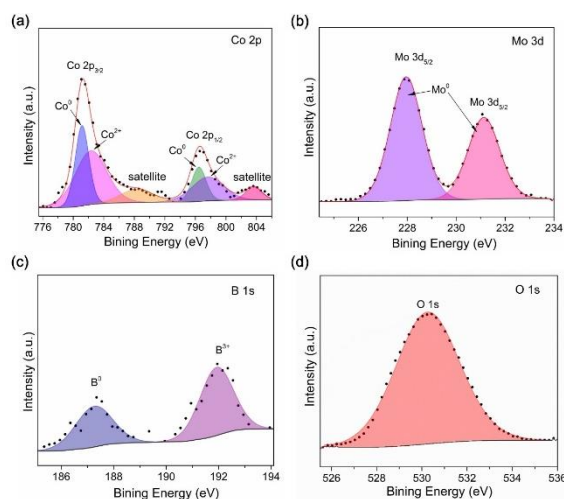


Figure 4. XPS spectra of Co 2p (a), Mo 3d (b), B 1s (c) and O 1s states

The HER performance of the Co-Mo-B/CC electrode are evaluated in N_2 -saturated 1.0 M KOH solution and compared with CC substrate, Co-B/CC electrode and the commercial Pt/C catalyst (Fig. 5). Fig. 3a displays LSV curves of the electrochemical HER. It is obvious that the CC substrate shows almost no HER activity under the applied potential range. As expected, the Co-Mo-B/CC electrode requires a much lower overpotential (η) of 84.5 mV to achieve a current density of 10 mA/cm^2 when compared with that of Co-B/CC electrode ($\eta_{10}=191 \text{ mV}$). It means that a synergistic effect exists in the ternary Co-Mo-B to promote the HER reaction. Besides, the catalytic currents of Co-Mo-B/CC electrode surpassed that of Pt/C/CC electrode at the overpotentials higher than 323 mV.

The Tafel slopes, drawn by plotting the logarithm of the reaction current density according to the Tafel equation [5], are employed to probe the reaction kinetics. As shown in Fig 5b, the Tafel slope of Co-B/CC and Co-Mo-B/CC electrodes are determined to be $152.8 \text{ mV dec}^{-1}$ and 98.2 mV dec^{-1} , indicating the dominance HER mechanism is a Volmer-Heyrovsky reaction pathway. While the Tafel slope of Pt/C/CC is 32.3 mV dec^{-1} , which is very close to the reported Pt/C catalyst [19]. In comparison with Co-B/CC electrode, Co-Mo-B/CC electrode owns smaller Tafel slope, suggesting its better HER kinetics, which together with the lower η_{10} makes it a highly efficient toward the HER.

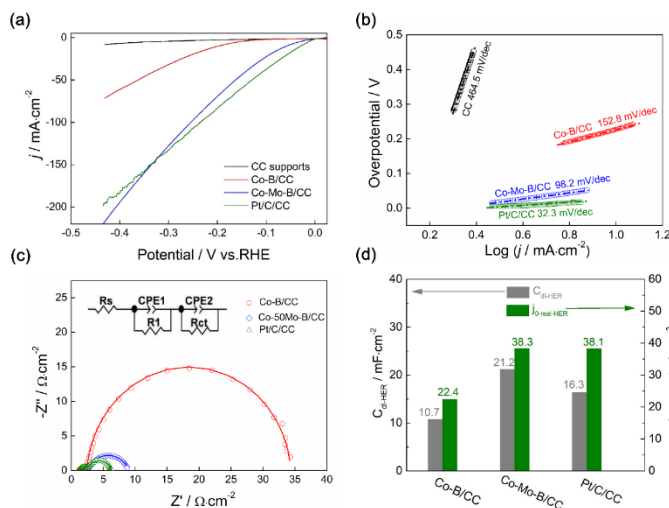


Figure 5. Electrocatalytic performance of HER: (a) LSV and (b) Tafel plots of the CC, Co-B/CC, Co-Mo-B/CC, Pt/C/CC electrodes; (c) EIS plots a of the Co-B/CC, Co-Mo-B/CC, Pt/C/CC electrodes at cathodic overpotential of 160 mV and the equivalent circuit mode (inset of c); (d) C_{dl} and j_{0-real} values of the Co-B/CC, Co-Mo-B/CC, Pt/C/CC electrodes.

EIS plots performed at the cathodic overpotential of 160 mV are carried out to further investigate insight into the charge transfer. The obtained Nyquist plots for all samples display two capacitive loops, containing low-frequency semicircle related to HER kinetics and high-frequency semicircle associated with the nature large specific surface area property of the CC supports electrodes [4]. Therefore, the 2TS model ($R_s-(R_1||CPE1)-(R_{ct}||CPE2)$) shown in the insert of Fig.5c is used to fit the Nyquist plots. Where, R_s , R_1 and R_{ct} are the solution resistance, porosity resistance and charge transfer resistance. CPE1 and CPE2 present the constant phase element for the porosity and HER process. The fitted lines presented in Fig.3c suggest good fitting quality and the results are listed in Table 1. The electrochemically active surface area (ECSA) can be evaluated based on the electrochemical double-layer ($C_{dl}=\{CPE2/[(R_s+R_1)^{-1}+R_{ct}^{-1}]^{(1-n_2)}\}^{1/n_2}$) [4]. As shown in Fig. 3d, the Co-Mo-B/CC electrode presents the largest C_{dl} (21.2 mF cm^{-2}), which is ~ 1.30 and ~ 1.98 times more than that of Pt/C/CC electrode (16.3 mF cm^{-2}) and Co-B/CC electrode (10.7 mF cm^{-2}), suggesting that Co-Mo-B/CC electrode owns a larger active surface area than the other two electrode and thus possess favorable catalytic performance. The other important indicator activity for catalysts, real exchange current density (j_{0-real}), is estimated by the equation $j_{0-real} = 20*j_0 / C_{dl}$ [2]. Where j_0 is the apparent exchange current density., the intrinsic high HER catalytic activity can be also reflected by its j_{0-real} (38.3 $\mu A cm^{-2}$) displayed in Fig. 3d, which is much bigger than that of Co-B/CC electrode (22.4 $\mu A cm^{-2}$), and close to the Pt/C/CC electrode (38.1 $\mu A cm^{-2}$).

Table 1. Parameters of the EIS measurements (HER, at overpotential of 160 mV)

Sample	R_s ($\Omega \cdot cm^2$)	CPE_1 (S sec^n)	n_1	R_1 ($\Omega \cdot cm^2$)	CPE_2 (S sec^n)	n_2	R_{ct} ($\Omega \cdot cm^2$)
Co-B/CC	1.905	0.0049	0.6168	3.092	0.0037	0.9575	53.370
Co-Mo-B/CC	1.746	0.0025	0.7488	0.799	0.0302	0.7569	6.476
Pt/C/CC	1.736	0.0054	0.6531	0.752	0.0220	0.7787	8.033

Although H_2 is generated by the cathodic HER process, anodic OER process is also critical because it is more sluggish and complex with higher overpotential [36]. In addition to the superior HER catalytic activity, Co-Mo-B/CC electrode also shows excellent OER performance. The OER catalytic activity is first examined by LSV curves and the corresponding Tafel slopes (Fig.6a-b). The LSV curves in Fig.4a demonstrate that Co-Mo-B/CC electrode possesses the highest OER activity with $\eta_{10}=192.6$ mV, outperforming those of Co-B/CC electrode (395.7 mV) and RuO_2/CC electrode (424.2 mV). In addition, Co-Mo-B/CC electrode exhibits a smaller Tafel slope value (87.5 mV dec^{-1}) in contrast to that of Co-B/CC electrode (134.6 mV dec^{-1}) and RuO_2/CC electrode (90.6 mV dec^{-1}), verifying the superiority of Co-Mo-B/CC electrode for OER kinetics in alkaline media.

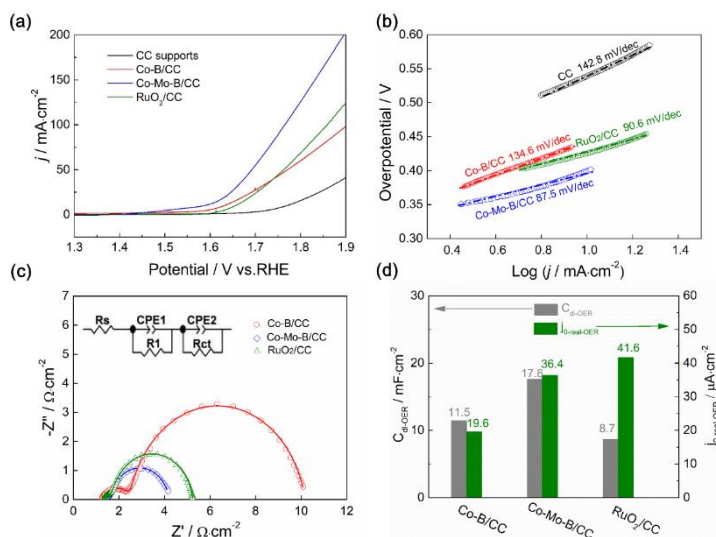


Figure 6. Electrocatalytic performance of OER: (a) LSV and (b) Tafel plots of the CC, Co-B/CC, Co-Mo-B/CC, RuO_2/CC electrodes; (c) EIS plots of the Co-B/CC, Co-Mo-B/CC, RuO_2/CC electrodes at cathodic overpotential of 280 mV and the equivalent circuit mode (inset of c); (d) C_{dl} and j_{0-real} values of the Co-B/CC, Co-Mo-B/CC, RuO_2/CC electrodes.

EIS plots are also employed to investigate the OER process and performed at the anodic overpotential of 280 mV. Fig.6c shows that the Nyquist plots can also be well fitted to the 2TS model. The fitted results are listed in Table 2 and the calculated C_{dl} and j_{0-real} are displayed in Fig.6d. It can be found that Co-Mo-B/CC electrode has the biggest C_{dl} value (17.6 mF cm^{-2}) and a relatively large j_{0-real} value (36.4 μA cm^{-2}), which is $\sim 87.5\%$ of that of RuO_2/CC electrode (41.6 μA cm^{-2}).

Table 2. Parameters of the EIS measurements (OER, at overpotential of 280 mV)

Sample	R_s ($\Omega \cdot cm^2$)	CPE_1 (S sec^n)	n_1	R_1 ($\Omega \cdot cm^2$)	CPE_2 (S sec^n)	n_2	R_{ct} ($\Omega \cdot cm^2$)
Co-B/CC	1.526	0.3196	0.9032	0.436	0.0824	0.5250	4.657
Co-Mo-B/CC	1.356	0.2489	0.8938	0.312	0.1541	0.4604	2.570
RuO_2/CC	1.522	0.0904	0.9293	0.539	0.0762	0.4766	8.491

Finally, the long-term cycling and steady-state chronopotentiometry electrode are carried out to evaluate the durability of Co-Mo-B/CC electrode, which is another critical criterion to assess catalysts for practical application. Obviously, , the η_{20} and η_{50} for HER increase by 3 mV and 7 mV, and the η_{20} and η_{50} for OER increase by 6 mV and 10 mV, respectively (Fig 7a-b). Meanwhile, there exist negligible increase of overpotentials after 36 h constant current running at the -10 mA cm^{-2} (for HER) and 10 mA cm^{-2} (for OER), displaying its favorable stability, as shown in Fig 7c-d.

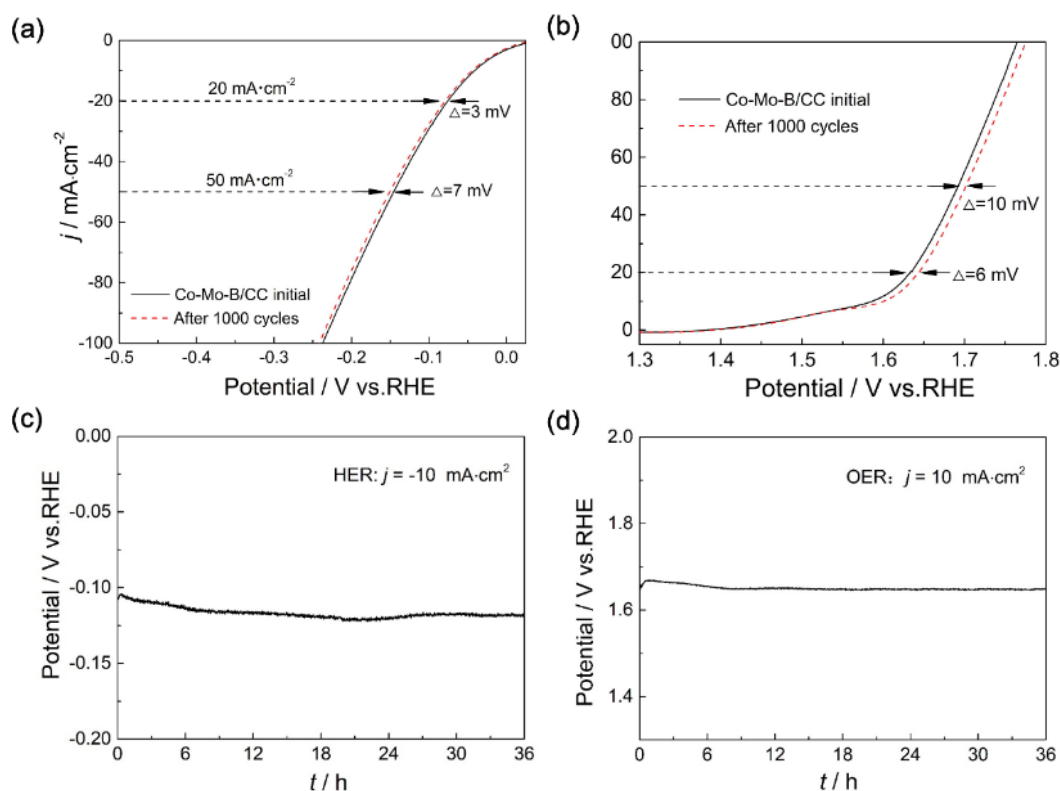


Figure 7. LSV curves of Co-Mo-B/CC electrode toward (a) HER and (b) OER before and after 1000 CV cycles, chronopotentiometry curves of Co-Mo-B/CC electrode toward (c) HER and (d) OER.

The LSV curves in Fig 8a show the Co-Mo-B/CC electrode can producing H₂ and O₂ efficiently in the respective potential regions, confirming its true bifunctional nature. In addition, the Co-Mo-B/CC electrode owns an approximate E_{overall} value in comparison with that of Pt/C/CC and RuO₂/CC couple at the reaction current density of 10 and 20 mA cm⁻². To demonstrate its practical applications, Co-Mo-B/CC has been utilized to serve as both anode and cathode in a two-electrode electrolysis system. It can be found that Co-Mo-B/CC(-)//Co-Mo-B/CC(+) only needs a cell voltage of 1.694 V to drive $j_{\text{cell}} = 10 \text{ mA cm}^{-2}$ for overall water splitting, being smaller than those of reported alkaline electrolyzer assembled by bifunctional electrocatalysts. Besides, the Co-Mo-B/CC(-)//Co-Mo-B/CC(+) exhibits excellent stability based on the negligible change of cell voltage at $j_{\text{cell}} = 10 \text{ mA cm}^{-2}$ over a period of 36 h (Fig 8b). From the above analysis, Co-Mo-B/CC electrode possess admirable catalytic activity and stability in alkaline solution. In addition, the cell voltage (at $j_{\text{cell}} = 10 \text{ mA cm}^{-2}$) of Co-Mo-B/CC(-)//Co-Mo-B/CC(+) is quite close to the most of those as-reported alkaline electrolyzer assembled by bifunctional

electrocatalysts [2, 6, 37-40]. It is anticipated that this Co-Mo-B/CC catalytic electrode, which possesses excellent performance and low cost and is fabricated via a simple, fast electrodeposition process, would have tremendous potential in commercial applications.

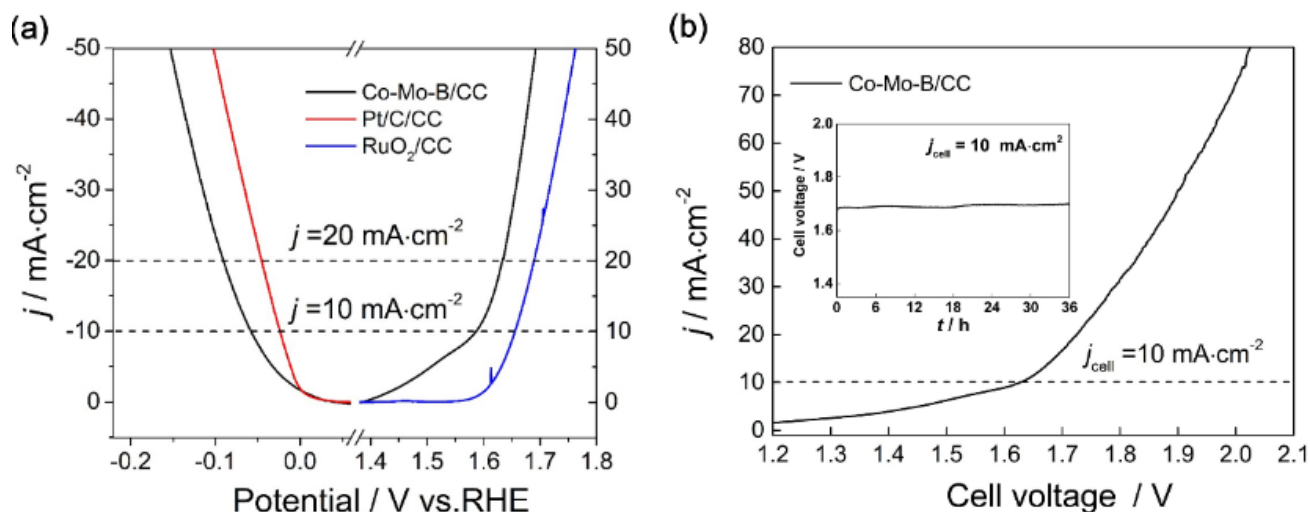


Figure 8. (a) LSV curves of Co-Mo-B/CC, Pt/C/CC electrode for HER (left) and Co-Mo-B/CC, RuO₂/CC for OER (right), (b) LSV curve of Co-Mo-B/CC(-) // Co-Mo-B/CC(+) for overall water splitting in a two-electrode configuration and the chronopotentiometry curve of Co-Mo-B/CC(-) // Co-Mo-B/CC(+) for water splitting at $j_{cell} = 10$ mA cm⁻² (the insets).

Table 3. Comparison of bifunctional electrocatalysts for water splitting performance in 1.0 M KOH

Catalysts (anode)	η (mV) @ j (mA·cm ⁻²)	Catalysts (cathode)	η (mV) @ j (mA·cm ⁻²)	Cell voltage (V) @ j (mA·cm ⁻²)	Ref. in text
Co-Mo-B/CC	192.6@10	Co-Mo-B/CC	84.5@10	1.694@10	This work
Co-W-P/CC	350@10	Co-W-P/CC	150@10	1.74@10	6
CTCP/CNTF	252@10	CTCP/CNTF	133@10	1.69@10	2
Mo ₂ C@CS	320@10	Mo ₂ C@CS	178@10	1.73@10	37
HP-TiO ₂ /Ni	309@10	HP-TiO ₂ /Ni	133@10	1.71@10	38
Fe-NiS ₂ /CF	243@20	Fe-NiS ₂ /CF	249@20	1.722@10	39
SNCF-NRs	370@10	SNCF-NRs	232@10	1.68@10	40

4. CONCLUSIONS

In summary, a self-supported catalytic electrode (Co-Mo-B/CC electrode) is fabricated by a facile electrodeposition technique. The nodular Co-Mo-B spheres with diameter of 80-100 nm and

amorphous nature compactly cover the entire surface of CC. The prepared Co-Mo-B/CC electrode exhibits outstanding electrocatalytic performance towards both HER and OER. For HER, it owns with small overpotentials (η) of 84.5 mV to sustain a cathodic current density of 10 mA cm², outperforming those of Co-B/CC electrode ($\eta_{10\text{-HER}}=191$ mV) and surpassing the Pt/C/CC electrode at high overpotentials (>323 mV). For OER, the Co-Mo-B/CC electrode possess a low $\eta_{10\text{-OER}}$ (192.6 mV), smaller than that of Co-B/CC electrode (395.7 mV) and RuO₂/CC electrode (424.2 mV). In addition, the two-electrode electrolysis system of Co-Mo-B/CC(-)//Co-Mo-B/CC(+) shows a quite low cell voltage of 1.694 V to drive $j_{\text{cell}} = 10$ mA cm⁻² for overall water splitting and admirable stability. This work showcases the possibility of fabricating composite self-supported electrode, including amorphous TMBs catalytic and the CC supports, in the area of the developing commercial high-performance non-noble metals based bifunctional catalysts for water splitting.

ACKNOWLEDGEMENTS

This work is financially supported by the National Natural Science Foundation of China (Grant No. 51764017), the Basic Research Program of Natural Science of Shaanxi Province (Grant No. 2019JQ-584), the National MCF Energy R&D Program (2018YFE0306105), and the Postgraduate Research & Practice Innovation Program of Jiangsu Province (KYCX19-1944).

References

1. Q. Zhou, T Fan, Y. Li, D. Chen, S. Liu, X. Li, *J. Power Sources*, 426 (2019) 111-115.
2. Q. Wu, M. Sheng, J. Shi, Q. Zhou, F. Liao, F. Lv, *Appl. Surf. Sci.*, 514 (2020) 145919.
3. S. Kendouli, S. Achour, N. Sobti, L. Chetibi, D. Hamana, *J. Mater. Eng. Perform.*, 29 (2020) 1-10.
4. Q. Zhou, S. Liu, Y. Zhang, Z. Zhu, W. Su, M. Sheng, *Ceram. Int.*, 46 (2020)20871-20877.
5. G. B. Darband, M. Aliofkhazraei, S. Hyun, A. S. Rouhaghdam, S. Shanmugam, *J. Power Sources*, 429 (2019) 156-167.
6. Q. Wu, T. Yao, M. Sheng, J. Shi, F. Lv, *Mater. Res. Express*, 6 (2019) 115507.
7. M. Manazoğlu, G. Hapçı, G. Orhan, *J. Mater. Eng. Perform.*, 25 (2016) 130-137.
8. D. Ding, K. Shen, X. Chen, H. Chen, J. Chen, T. Fan, R. Wu, Y. Li, *ACS Catal.*, 8 (2018) 7879-7888.
9. L. Elias, K. Scott, A. C. Hegde, *J. Mater. Eng. Perform.*, 24 (2015) 4182-4191.
10. J. Tian, N. Cheng, Q. Liu, X. Sun, Y. He, A. M. Asiri, *J. Mater. Chem. A*, 3 (2015) 20056-20059.
11. K. N. Dinh, Q. Liang, C. F. Du, J. Zhao, A. I. Y. Tok, H. Mao, Q. Yan, *Nano Today*, 25(2019) 99-121.
12. W. Lu, T. Liu, L. Xie, C. Tang, D. Liu, S. Hao, F. Qu, G. Du, Y. Ma, A. M. Asiri, X. Sun, *Small*, 13 (2017) 1700805.
13. Y. Liang, X. Sun, A. M. Asiri, Y. He, *Nanotechnology*, 27 (2016) 12LT01.
14. J. H. Kim, D. H. Youn, K. Kawashima, J. Lin, H. Lim, C. B. Mullins, *Appl. Catal. B.*, 225 (2018) 1-7.
15. S. Wang, P. He, Z. Xie, L. Jia, M. He, X. Zhang, F. Dong, H. Liu, Y. Zhang, C. Li *Electrochim. Acta*,296 (2019) 644-652.
16. H. Chen, S. Ouyang, M. Zhao, Y. Li, J. Ye, *ACS Appl. Mater. Interfaces*, 9 (2017) 40333-40343.
17. T. Rauscher, C. I. Müller, A. Schmidt, B. Kieback, L. Röntzsch, *Int. J. Hydrogen. Energy*, 41 (2016) 2165-2176.
18. S. Gupta, N. Patel, R. Fernandes, S. Hanchate, A. Miotello, D. C. Kothari, *Electrochim. Acta*, 232 (2017) 64-71.
19. Y. Zou, Y. Yin, Y. Gao, C. Xiang, H. Chu, S. Qiu, E. Yan, F. Xu, L. Sun, *Int. J. Hydrogen Energy*, 43 (2018) 4912-4921.

20. S. Nardecchia, D. Carriazo, M.L. Ferrer, M.C. Gutiérrez, F. del Monte *Chem. Soc. Rev.*, 42 (2013) 794–830.
21. T. N. J. I. Edison, R. Atchudan, N. Karthik, M. G. Sethuraman, Y. R. Lee, *J. Taiwan Inst. Chem. Eng.*, 80 (2017)901-907.
22. J. Wang, D. Ke, Y. Li, H. Zhang, C. Wang, X. Zhao, Y. Yuan, S. Han, *Mater. Res. Bull.*, 95 (2017) 204-210.
23. H. Sun, Z. Yan, F. Liu, W. Xu, F. Cheng, *Adv. Mater.*, 32 (2020) 1806326.
24. C. Yang, M. Y. Gao, Q. B. Zhang, J. R. Zeng, X. T. Li, A. P. Abbott, *Nano Energy*, 36 (2017) 85-94.
25. P. Jiang, Q. Liu, X. Sun, *Nanoscale*, 6 (2017) 13440-13445.
26. P. Wang, F. Song, R. Amal, Y. H. Ng, X. Hu, *ChemSusChem*, 9 (2016) 472-477.
27. W. Fang, D. Liu, Q. Lu, X. Sun, A. M. Asiri, *Electrochem Commun.* 63 (2016) 60-64
28. C. Xiang, J. Cheng, Z. She, Y. Zou, H. Chu, S. Qiu, H. Zhang, L. Sun, F. Xu, *RSC Adv*, 5 (2015) 163-166
29. H. Alimadadi, M. Ahmadi, M. Aliofkhazraei, S.R. Younesi, *Mater. Des.*, 30(2009) 1356-1361
30. Z. Sun, S. Hao, X. Ji, X. Zheng, J. Xie, X. Li, B. Tang, *Dalton. Trans.*, 47 (2018) 7640-7643
31. J. Xie, Y. Xie, *ChemCatChem*, 7 (2015) 2568-2580.
32. L. Shi, Z. Chen, Z. Jian, F. Guo, C. Gao, *Int. J. Hydrogen. Energy*, 44 (2019) 19868-19877.
33. W. Li, D. Xiong, X. Gao, W. G. Song, F. Xia, L. Liu, *Catal. Today*, 287 (2017) 122-129
34. Y. Ito, T. Ohto, D. Hojo, M. Wakisaka, Y. Nagata, L. Chen, T. Adschiri, *ACS Catal.*, 8 (2018) 3579-3586
35. J. Sun, W. Zhang, S. Wang, Y. Ren, Q. Liu, Y. Sun, L. Tang, J. Guo, X. Zhang, *J. Alloys Compd.*, 776 (2019) 511-518
36. X. Li, H. Wang, Z. Cui, Y. Li, S. Xin, J. Zhou, Y. Long, C. Jin, J. B. Goodenough, *Sci. Adv.*, 5 (2019) eaav6262.
37. L. L. Zhu, H. P. Lin, Y. Y. Li, F. Liao, Y. Lifshitz, M. Q. Sheng, S. T. Lee, M. W. Shao, *Nat. Commun.*, 7 (2016) 1–7.
38. D. Y. Kuo, H. J. Paik, J. Kloppenburg, B. Faeth, K. M. Shen, D. G. Schlom, G. Hautier, J. Suntivich, *J. Am. Chem. Soc.*, 140 (2018) 17597–17605.
39. M .Q. Sheng, B. B. Jiang, B. Wu, F. Liao, X. Fan, H. P. Lin, Y. Y. Li, Y. Lifshitz, S. T. Lee, M. W. Shao, *ACS Nano*, 13 (2019) 2786–2794.
40. C. Yu, H. W. Huang, S. Zhou, X. T. Han, C. T. Zhao, J. Yang, S. F. Li, W. Guo, B. W. An, J. J. Zhao, J. S. Qiu, *Nano Res.*, 11 (2018) 3411–3418.